PROCEEDINGS OF SPIE

SPIEDigitalLibrary.org/conference-proceedings-of-spie

# Influence of water waves on hyperspectral remote sensing of subsurface water features

Charles R. Bostater
Luce Bassetti

SPIE.

# Influence of Water Waves on Hyperspectral Remote Sensing of Subsurface Water Features

Charles R. Bostater, Jr.[1], Luce Bassetti
Marine Environmental Optics Laboratory & Remote Sensing Center
College of Engineering
Florida Institute of Technology
Melbourne, Florida

## ABSTRACT

Modeled hyperspectral reflectance signatures with water wave influences are simulated using an analytical-based, iterative radiative transport model applicable to shallow or deep waters. Light transport within the water body is simulated using a fast, accurate radiative transfer model that calculates the light distribution in any layered media and incorporates realistic water surfaces which are synthesized using empirically-based spectral models of the water surface to generate water surface wave facets. The model simulated synthetic images are displayed as 24 bit RGB images of the water surface using selected channels from the simulated synthetic hyperspectral image cube. We show selected channels centered at 490, 530 and 676 nm. We also demonstrate the use of the model to show the capability of the sensor and image modeling approach to detect or "recover" known features or targets submerged within or on the shallow water bottom in a tidal inlet area in Indian River Lagoon, Florida. Line targets are simulated in shallow water and indicate the influence of water waves in different water quality conditions. The technique demonstrates a methodology to help to develop remote sensing protocols for shallow water remote sensing as well as to develop information useful for future hyperspectral sensor system developments.

**Keywords**: hyperspectral remote sensing, submerged targets, synthetic images, synthetic signatures, modeling, simulation, water surface reflectance, optically shallow water, hydrologic optics, radiative transfer, water surface waves, hyperspectral image cubes, submerged water features, environmental remote sensing, submerged vegetation monitoring, shallow water remote sensing, sensor simulation.

## 1. BACKGROUND

A "synthetic image" is defined a as simulated image, in contrast to a real or actual image obtained from a sensor. In this research, synthetic imaging of shallow water is demonstrated using a simulated line target with our analytical radiative transfer model with realistic water surface waves. The synthetic hyperspectral images can be compared to actual images obtained from an imaging system on an aircraft or satellite to assess the accuracy of remote sensing algorithms. The purpose of generating these synthetic images is to use the images in water quality research and for algorithm testing useful in target recognition

[1] For Further Information: (Send correspondence to Dr. Bostater) Charles R. Bostater Jr., Director Marine and Environmental Optics Lab & Remote Sensing Center, College of Engineering, Florida Institute of Technology, Melbourne, Florida, US, 32937 email: bostater@probe.ocn.fit.edu Ph:321-258-9134, Fax: 321-600-9412.



Remote Sensing of the Ocean and Sea Ice 2004, edited by Charles R. Bostater, Jr., Rosalia Santoleri, Proceedings of SPIE Vol. 5569 (SPIE, Bellingham, WA, 2004)
0277-786X/04/$15 · doi: 10.1117/12.565273

in shallow waters. The purpose of this paper is to demonstrate and understand how different water types, bottom reflectance's (targets) , and constituent concentrations (or water quality indicators) cause differences in remote sensing images of the water surface reflectance, in the presence of a random water surface sea state. These results can be compared to Monte Carlo radiative models developed at our lab.
The ocean surfaces generated in this paper are based on the inverse fast Fourier transform (IFFT) methodology introduced by Mastin et al.[1] and developed further by Tessendorf, [2] Premoze and Ashikhmin,[3] and Jensen and Golias[4], and tutorials based upon the use of the IFFT methodology for generating ocean surface waves by Chen,[5] and Hilgart.[6]

## 2. GENERAL METHODS

The general steps for generating a synthetic image using our analytical radiative transfer model with realistic water surfaces include the following general steps. First, for representation of the reflectance model image, the horizontal dimensions (x and y directions) in meters as well as the number of discrete sample points or pixels in each direction are selected, next the atmospheric attenuation model of Gregg and Carder[7] is used to calculate the direct and diffuse downwelling light at the top of the sea surface. Since the area modeled is on the order of meters, it is assumed that the downward direct and diffuse components of irradiance at the top of the sea surface are the same for all pixels. Third, water wave surface based on the IFFT methodology[1,2,3,4,5,6] is generated for the horizontal dimensions and number of pixels chosen in the first step above. Next the reflectivity and transmittance of the direct and diffuse irradiance at the air-sea interface are calculated for each pixel using Snell's and Fresnel's equations. Then, water quality parameters and depth values for each pixel are input from a set of files. These water quality parameters include the specific absorption coefficient for pure water, the specific absorption coefficient for chlorophyll, the specific absorption coefficient for suspended sediment (SS), the specific absorption coefficient for dissolved organic matter (DOM), the specific backscattering coefficient for pure water, the specific backscattering coefficient for chlorophyll, the specific backscattering coefficient for suspended sediment (SS), the concentration of chlorophyll, the concentration of suspended sediment (SS), the concentration of dissolved organic matter (DOM), and the depth of the water column at each pixel or location within the image domain to be simulated. For the iterative, layered, analytical radiative transfer model, a model run is used to calculate the water volume effect on reflectance for each pixel, or the subsurface reflectance, or the upwelling irradiance and radiance. Then, steps four through six are repeated to simulate reflectance values for each required wavelength. Image-processing software is then used to import three bands in order to display the RGB image. Relevant details are provided for the steps three through six below. Downward irradiance at the sea surface is affected by reflection and refraction at the air-sea interface. The Snell and Fresnel laws describe the reflection and refraction of light at the interface between two media such as the atmosphere and sea surface. The reflections of direct and diffuse downwelling irradiance on the sea surface are the specular surface reflectance ($R_S$) and the diffuse surface reflectance ($R_d$) respectively. Each reflectance can be separated into two terms, a specular reflectance component, and reflectance due to sea foam[8]. These relationships are given by:

$$R_s(\theta, w_s) = \rho_{fres}(\theta) + \rho_f(w_s) \quad , \tag{1}$$

$$R_d(w_s) = \rho_d(w_s) + \rho_f(w_s) \quad , \tag{2}$$

where the subscripts "fres ", "d", and " f " refer to specular direct reflectance calculated from the Fresnel reflectance formula (equation 20), specular diffuse reflectance, and foam reflectance. $\theta$ represents the incident and reflection angles with respect to the normal vector of the wave facet slope and $w_s$ represents the wind speed (m/s). The specular surface reflectance, $R_s$, on the sea surface can be calculated from the Snell and Fresnel Laws if the surface normal direction for each pixel, the solar angle, the observation

angle, and the index of refraction of air and seawater are specified. In order to obtain the surface normal direction for each pixel, it is necessary to generate the surface slopes using the IFFT methodology, where in Fourier transform theory there are two domains, the "frequency domain" and the "space (and time) domain". The Fourier transform is used to move between the two domains. Transforms from the space domain to the frequency domain are forward Fourier transforms. Transforms from the frequency domain to the space domain are inverse Fourier transforms. In the frequency domain, there is one complex value for each discrete frequency which provides information about the relative contribution to the wave amplitude by each discrete frequency. The IFFT based representation of a wave height field (z-direction) expresses the wave height h(**x**, t) at the horizontal position x = (x, y) as the sum of sinusoids with complex time-dependent amplitudes[2,4]:

$$h(\mathbf{x},t) = \sum_{k} \tilde{h}(\mathbf{k},t)\exp(i\mathbf{k}\cdot\mathbf{x}) \quad , \tag{3}$$

where $h(\mathbf{x},t)$ is the wave height at the horizontal position $\mathbf{x} = (x,z)$ at time t, $\mathbf{k}$ is a two-dimensional vector pointing in the direction of travel of a given wave, with a magnitude $|\mathbf{k}|$ dependent on wavelength $\lambda$, $(k = 2\pi/\lambda)$, and $\tilde{h}(\mathbf{k},t)$ is a complex number representing the amplitude and phase of wave $\mathbf{k}$ at time t. The components of $\mathbf{k}$ are calculated using equations (6) and (7) below. In order to create the initial array of complex numbers at time t=0 needed for the IFFT algorithm, Tessendorf [2] suggests using the Phillips spectrum to generate the initial amplitudes and phases of the waves. The Phillips spectrum was developed from statistical analysis of wave-buoy, photographic, and radar measurements of the ocean surface. [2] Other surface wave generating models used to create this initial array of complex numbers include the JONSWAP (Joint North Sea Wave Project) spectrum used by Premoze and Ashikhmin[3] to create their synthetic images of natural water. The Phillips spectrum model for wind-driven waves in a fully developed sea is defined by: [2,4,5,6]

$$\tilde{h}_0(\mathbf{k}) = \frac{1}{\sqrt{2}}(\varepsilon_r + i\varepsilon_i)\sqrt{P_h(\mathbf{k})}, \tag{4}$$

$$P_h(\mathbf{k}) = A\frac{\exp\left(-1/(kL)^2\right)}{k^4}\left|\hat{\mathbf{k}}\cdot\hat{w}\right|^2 \exp\left(-k^2l^2\right), \tag{5}$$

where $\tilde{h}_0(\mathbf{k})$ is the initial height field (a complex number) generated from the statistically derived Phillips spectrum, $\varepsilon_r$ and $\varepsilon_i$ are Gaussian random numbers, $A$ is a numeric constant for the wave height scale (common values are between 0.0005 and 0.00000375), k is the magnitude of $\mathbf{k}$, the two-dimensional vector pointing in the direction of travel of a given wave, $L$ determines the size of the largest possible wave for a given wind speed ($L = \frac{w_s^2}{g}$ where $w_s$ is the wind velocity in m/s and g is the gravitational constant in m/s$^2$), $\hat{\mathbf{k}}$ is the normalized direction vector of a given wave $\frac{\mathbf{k}}{|\mathbf{k}|}$, $\hat{w}$ is the normalized direction of the wind, and the term $\exp\left(k^2l^2\right)$ is a damping factor to suppress waves with very small wavelength. The damping factor can also be modified to $\exp\left(k^6l^6\right)$ to more strongly align the waves with the wind direction[2]. The factor $l$ should typically be at least 10 times smaller than the value of $L$. The wave direction vector $\hat{\mathbf{k}}$ is calculated as follows:

$$k_x = \left(-\frac{M}{2} + m\right) * \left(\frac{2\pi}{L_{wx}}\right) \quad , \tag{6}$$

$$k_y = \left( -\frac{N}{2} + n \right) * \left( \frac{2\pi}{L_{wy}} \right) \quad , \tag{7}$$

"m" and "n" are the row and column of the $\tilde{h}_0$ array. $L_{wx}$ and $L_{wy}$ are the horizontal dimensions (m) of the "wave patch" that the IFFT algorithm produces. The "wave patch" size generally varies from 10 m to 2000 m on a side.[2] M and N are the number of discrete sample points or pixels within this "wave patch". M and N should be in a power of 2 and range between 16 and 2048.[2] The "wave patch" can be tiled, if desired, to simulate a larger sea surface area. The values $\frac{L_{wx}}{M}$ and $\frac{L_{wy}}{N}$ are the dimension of the smallest wave facet in either direction. Below these scales, the amount of wave action is small compared to the rest of the waves therefore according to Tessendorf [2], the values of $\frac{L_{wx}}{M}$ and $\frac{L_{wy}}{N}$ should be at least 10 to 1000 times smaller than $L = \frac{w_s^2}{g}$ or most of the " interesting" waves will be lost.[2]

Once the initial height field $\tilde{h}_0(\mathbf{k})$ at time t=0 is created, the second step required to prepare for the IFFT is to phase shift the $\tilde{h}_0$ array. The frequency amplitudes of the wave field at time t, given a dispersion relation $\omega^2(\mathbf{k}) = g\mathbf{k}\tan\theta$ are described by: [2, 6]

$$\tilde{h}(\mathbf{k},t) = \tilde{h}_0(\mathbf{k})\exp(i\omega(k)t) + \tilde{h}_0^*(-\mathbf{k})\exp(-i\omega(k)t) \quad , \tag{8}$$

where $\tilde{h}(\mathbf{k},t)$ are the frequency amplitudes of the wave field at time t, $\omega(k)$ is the speed at which wave $\mathbf{k}$ travels across the water surface, and $\tilde{h}_0^*(\mathbf{k})$ employs the complex conjugate property such that $\tilde{h}^*(\mathbf{k},t) = \tilde{h}(-\mathbf{k},t)$. [2,4] What the complex conjugate does, is to negate the imaginary component of $\tilde{h}_0(\mathbf{k})$ so that transforming from the frequency domain to the space domain, all points are reflected as real numbers. Through Euler's formula, a complex number such as $\exp(i\omega(k)t)$ can be written as:

$$\cos(\omega(k)t) + i\sin(\omega(k)t), \tag{9}$$

where, for deep water, the dispersion relation $\omega(k) = gk$ is used, and for shallow water the dispersion relation can be modified to $\omega(k) = gk\tanh(kd)$ where d is the water depth. Next, equation (8) is broken into four parts (shown as equations 10, 11, 12, and 13) using Euler's formula (equation 9). Note that p, q, r, and s are all complex numbers, q is the complex conjugate of p, s is the complex conjugate of r, m and n are the row and column of the $h_0$ array, and mm and nn are also the row and column in the $h_0$ array where mm is the remainder or modulus of m/M and nn is the remainder or modulus of n/N.

$$p = \tilde{h}_0(\mathbf{k}) = h_0(m,n) + ih_0(m,n), \tag{10}$$

$$q = \tilde{h}_0(-\mathbf{k}) = h_0(mm,nn) - h_0(mm,nn), \tag{11}$$

$$r = \cos(\omega(k)t) + i\sin(\omega(k)t), \tag{12}$$

$$s = \cos(\omega(k)t) - i\sin(\omega(k)t). \tag{13}$$

The complex frequency amplitudes to be input to the IFFT subroutine are calculated by:

$$(p*r) + (q*s). \tag{14}$$

Substituting equations 10 through 13 into equation 14 and expanding, we obtain equation 15 as follows:

$$\begin{aligned}\tilde{h}(\mathbf{k},t) &= \left(h_0(m,n)+ih_0(m,n)\right)*\left(\cos\left(\omega(k)t\right)+i\sin\left(\omega(k)t\right)\right)+\\ &\left(h_0\left(mm,nn\right)-h_0\left(mm,nn\right)\right)*\left(\cos\left(\omega(k)t\right)-i\sin\left(\omega(k)t\right)\right)\\ &= h_0(m,n)\cos\left(\omega(k)t\right)+ih_0(m,n)\sin\left(\omega(k)t\right)+ih_0(m,n)\cos\left(\omega(k)t\right)\\ &\quad+i^2h_0(m,n)\sin\left(\omega(k)t\right)+h_0(mm,nn)\cos\left(\omega(k)t\right)-ih_0(mm,nn)\sin\left(\omega(k)t\right)\\ &\quad-ih_0(mm,nn)\cos\left(\omega(k)t\right)+i^2h_0(mm,nn)\sin\left(\omega(k)t\right)\quad.\end{aligned} \tag{15}$$

Noting that $i^2 = -1$, equation 15 can be further simplified to:

$$\tilde{h}(\mathbf{k},t) = \overbrace{\begin{aligned}&h_0(m,n)\left(\cos\left(\omega(k)t\right)-\sin\left(\omega(k)t\right)\right)\\&+h_0(mm,nn)\left(\cos\left(\omega(k)t\right)-\sin\left(\omega(k)t\right)\right)\end{aligned}}^{\text{real part}} + i\overbrace{\begin{bmatrix}h_0(m,n)\left(\cos\left(\omega(k)t\right)+\sin\left(\omega(k)t\right)\right)\\-h_0(mm,nn)\left(\cos\left(\omega(k)t\right)+\sin\left(\omega(k)t\right)\right)\end{bmatrix}}^{\text{imaginary part}}. \tag{16}$$

The IFFT subroutine is now run to convert the frequency amplitudes of the wave field $\tilde{h}(\mathbf{k},t)$ back to the space domain. To obtain the wave field in the space domain, a calculation of the gradient of the height field to find the surface normals is required. The algorithm for this paper is a finite difference method between adjacent grid points where:

$$\begin{aligned}-\frac{dh}{dx} &= \left(Height\left(m-1,n+1\right)+2*Height\left(m,n+1\right)+Height\left(m+1,n+1\right)\right)\\ &\quad-\left(Height\left(m-1,n-1\right)+2*Height\left(m,n-1\right)+Height\left(m+1,n-1\right)\right)\quad,\end{aligned} \tag{17}$$

$$\begin{aligned}-\frac{dh}{dy} &= \left(Height\left(m+1,n-1\right)+2*Height\left(m+1,n\right)+Height\left(m+1,n+1\right)\right)\\ &\quad-\left(Height\left(m-1,n-1\right)+2*Height\left(m-1,n\right)+Height\left(m-1,n+1\right)\right)\quad,\end{aligned} \tag{18}$$

The finite difference method can be a poor approximation of slope if wavelengths are small. [2] A reportedly more accurate approach for finding the normals is through more IFFTs (one in each direction) as follows: [2]

$$\nabla h(\mathbf{x},t) = \sum_k i\mathbf{k}\tilde{h}(\mathbf{k},t)\exp\left(i\mathbf{k}\cdot\mathbf{x}\right). \tag{19}$$

The angle θ which represents both the incident and reflection angles with respect to the normal vector of the wave facet slope is found by taking the dot product between the incident vector and the normal vector of the wave facet which is determined by the "assumed sensor" (or observation) zenith and azimuth angles and the "assumed sun" (or incident) zenith and azimuth angles for each pixel, relative to each pixel's position to the sensor and the sun. The Fresnel values for each pixel are calculated using the Snell and Fresnel laws shown in equations 20 and 21:

$$\rho(\theta) = 0.5*\left[\frac{\sin^2\left(\theta-\theta_r\right)}{\sin^2\left(\theta+\theta_r\right)}+\frac{\tan^2\left(\theta-\theta_r\right)}{\tan^2\left(\theta+\theta_r\right)}\right], \tag{20}$$

$$\theta_r = \sin^{-1}\left[\frac{\sin\theta*n_a}{n_w}\right], \tag{21}$$

where $\theta_r$, is the refracted angle, $n_a$ and $n_w$ are the refractive index of the air (assumed to be 1) and the water (assumed to be 1.34) respectively. Sea foam reflectance, $\theta_f$, is a function of sea-surface roughness,

and it is also a function of wind speed and wind stress.[8] Using the observations made by Koepke[8] and Gregg and Carder[7], Ma[9] developed the following relationship (Table 1) between sea foam reflectance ($\rho_f$) and wind speed.

Table 1. Relationship between wind speed and sea foam reflectance.[3,8,9]

| Wind speed, $W_s$ (m/s) | Sea foam reflectance, $\rho_f$ |
|---|---|
| $0 = W_s = 4$ | 0 |
| $4 < W_s = 7$ | $\rho_f = 2.2X10^{-5}\ \rho_a\ C_D\ w_s^2 - 4.0X10^{-4}$<br>$C_D = 6.2X10^{-4} + 1.56X10^{-3}/w_s$ |
| $W_s > 7$ | $\rho_f = (4.5X10^{-5}\ \rho_a\ C_D - 4.0X10^{-5})\ w_s^2$<br>$C_D = 4.9X10^{-4} + 6.5X10^{-5}\ w_s$ |

Note: $\rho_a$, is the density of air = $1.2X10^3$ g $m^{-3}$ and $C_D$ is the drag coefficient.

Using equation 1 to add the specular direct reflectance, $\rho(\theta)$, to the sea foam reflectance, $\rho_f(w_s)$, the specular surface reflectance, $R_s(\theta, w_s)$, is acquired. The transmittance of specular irradiance, $T_s(\theta, w_s)$, which is the proportion of the specular irradiance transmitted through the air-water surface, is calculated by:

$$T_s(\theta, w_s) = 1 - R_s(\theta, w_s). \tag{22}$$

The transmittance is used to calculate the specular irradiance just below the wind-roughened sea surface. The diffuse specular reflectance at the sea surface, $\theta_d$, is independent of incident angle$\theta$. If a smooth water and clear sky are assumed, then:

$$\rho_d = \int_{\phi=0}^{2\pi} \int_{\theta=0}^{\pi/2} \rho(\theta) \cos\theta \sin\theta d\theta d\phi \quad , \tag{23}$$

where $\rho(\theta)$ is the Fresnel reflectance. Numerical integration using Simpson's method is used to calculate the value $\theta_d$ = 6.7% ($\theta_d$ = 5.2 % under an overcast sky.[10]). This value is about the same value as calculated by Jerlov[11] and Preisendorfer,[12] for the index of refraction of sea water $n_w$ = 1.341. For a wind-roughened surface ($w_s$ > 4 m/s), the $\theta_d$ decreases to 0.057 due to wave breaking at wind speeds of approximately 4 to 5 m/s.[13] The sea foam reflectance can thus be added to the external diffuse reflectance using equation 2 to obtain the diffuse surface reflectance, $R_d(w_s)$. The transmittance of diffuse irradiance, $T_d(w_s)$ , which is the proportion of the diffuse irradiance transmitted through the air-water surface, is calculated by:

$$T_d(w_s) = 1 - R_d(w_s) \quad , \tag{24}$$

The transmittance is used to calculate the diffuse irradiance just below the wind-roughened sea surface. At this point, since the amount of direct and diffuse irradiance just below the sea surface for each pixel has been calculated, one must calculate the reflectivity of the water volume itself. In this paper, the water volume reflectivity is calculated by solving the radiative transfer equation in the form of the layered two-flow equations. The analytical solutions to the two-flow equations used in this research are an extension of those developed and advanced by Bostater and Lamb[3], Bostater, Ma *et al*,[14], Bostater, Ma, and McNally,[15] and modified to their present layered forms by Bostater and Huddleston,[16] Bostater, *et al*,[17].and Bostater, *et al*[18]. The forms of the two-flow equations solved are as follows:

$$\frac{dE_d(z)}{dz} = -(a+b)E_d(z) + bE_u(z) + cE_s(z), \tag{25}$$

$$\frac{dE_u(z)}{dz} = (a+b)E_u(z) - bE_d(z) - cE_s(z), \tag{26}$$

$$\frac{dE_s(z)}{dz} = -\alpha E_s(z), \tag{27}$$

where z=water depth in meters (m), positive downward, z=0 at the surface (m), $E_d(z)$ is the downwelling diffuse irradiance in the water column at depth z, $E_u(z)$ is the upwelling diffuse irradiance in the water column at depth z, $E_s(z)$ is the downwelling direct or collimated irradiance in the water column at depth z, a is the total absorption coefficient for a homogeneous layer of water ($m^{-1}$) , b is the total backscattering coefficient for a homogeneous layer of water ($m^{-1}$) , c is the conversion coefficient of direct to diffuse irradiance for a homogeneous layer of water ($m^{-1}$), and $\alpha$ is the diffuse beam attenuation coefficient for a homogeneous layer of water ($m^{-1}$). Although not explicitly shown, equations 25, 26, and 27 are assumed to be wavelength ( $\lambda$ ) dependent.

For a layered water column or layered media, the two-flow equations (equations 19, 20, and 21) cannot be solved by using the Cauchy boundary conditions employed by Bostater, *et al*.[14,15] This is because the upwelling irradiance at the bottom of each layer is not known until the downwelling diffuse and direct irradiance reach the bottom (h) of the water column. This limitation can be overcome by solving the solution to the two-flow equations iteratively. The amount of downwelling light backscattered in each layer, the amount of upwelling light backscattered in each layer, and the amount of collimated light that is converted to diffuse light are independently calculated. In order to calculate the downwelling irradiance at the next layer interface, the downwelling irradiance in the top of the layer is added to the amount of upwelling light backscattered into this layer and the amount of collimated light converted to diffuse downwelling light in this layer. The upwelling light in each layer is determined in the same manner. Figures 4 and 5 show example water column calculations and boundary conditions for downwelling and upwelling irradiance respectively. The subscripts on $a_i$, $b_i$, $c_i$, $m_i$, $n_i$, $\psi_i$, and $\alpha_i$ indicate the layer number (e.g. 1 or 2). The superscripts on $E_d^i$, $E_s^i$, and $E_u^i$, also indicate the layer number. The subscripts d, s, and u indicate downwelling, specular and upwelling irradiance. The numbers in parentheses indicate the depth of the current layer in meters (e.g. 0 m, 2.5 m, 5 m). The variable, $\psi_i$, is a second order attenuation coefficient for a homogeneous layer of water calculated by $\sqrt{a^2+2ab}$ . The variables m and n for a homogeneous layer of water are calculated by $-\frac{c(\alpha+a+2b)}{(\alpha^2-\psi^2)}E_s(0)$ and $-\frac{c(a+2b-\alpha)}{(\alpha^2-\psi^2)}E_s(0)$ respectively.

The influence of water waves on bottom features and submerged target like objects can be demonstrated as shown below by the influence of water waves on a simple line target. Figure 1 shows a line target above the water (left and submerged to an approximately 1.5 meter water depth, with small gravity waves and capillary waves driven by a wind speed less than 5 knots. The motivation for the modeling results and procedures described above and shown below is to attempt to quantify the influence of these waves on remote sensing images collected from airborne sensors flying at relatively low altitudes.

Figure 1. Line image target above (left) the water surface and below (right) the water surface. The water depth of the submerged target is approx. 1.5 m depth with winds less than 5 knots demonstrating the influence of small gravity and capillary waves on bottom feature and target recognition and identification. The methodology demonstrated is used to simulate or retrieve such features and targets from synthetic hyperspectral imagery.

A schematic diagram indicating the approach for simulating the water column in shallow waters with a bottom reflectance characteristic for each pixel and a water facet is shown in Figure 2 below. He approach is the same for the layered (ALIM) model or the Monte Carlo (MC) model results.

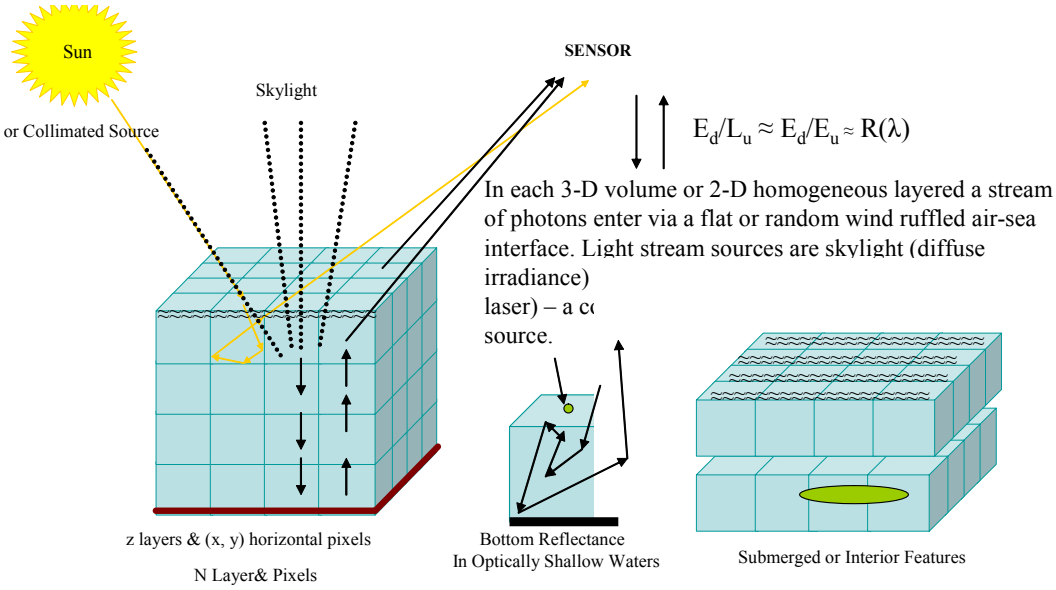


Figure 2. Schematic of the 3-D dimensional MCM (Monte Carlo Model) and the ALIM (Analytical Layered Iterative Model). Both models account for wavelength dependent bottom reflectance, water depth, absorption and scattering, BRDF (bidirectional reflectance due to the solar zenith angle of the sun and viewing angle of a sensor. Both models account for absorption and scattering (backscattering) due to constituents in the water column. The MC model accounts the influence of scattering shape factor effects.

Figures 3 and 4 below show the methods for calculation procedure for obtaining the irradiance downwelling and upwelling within and from the water column for each pixel of a synthetic image. The methods described above are combined with simulations of the irradiance within and just above the water surface, where we simulate the irradiance as shown below. Results from these simulations allow the

calculation of the simulated pixel by pixel reflectance signatures with the effects of the water surface as described above.

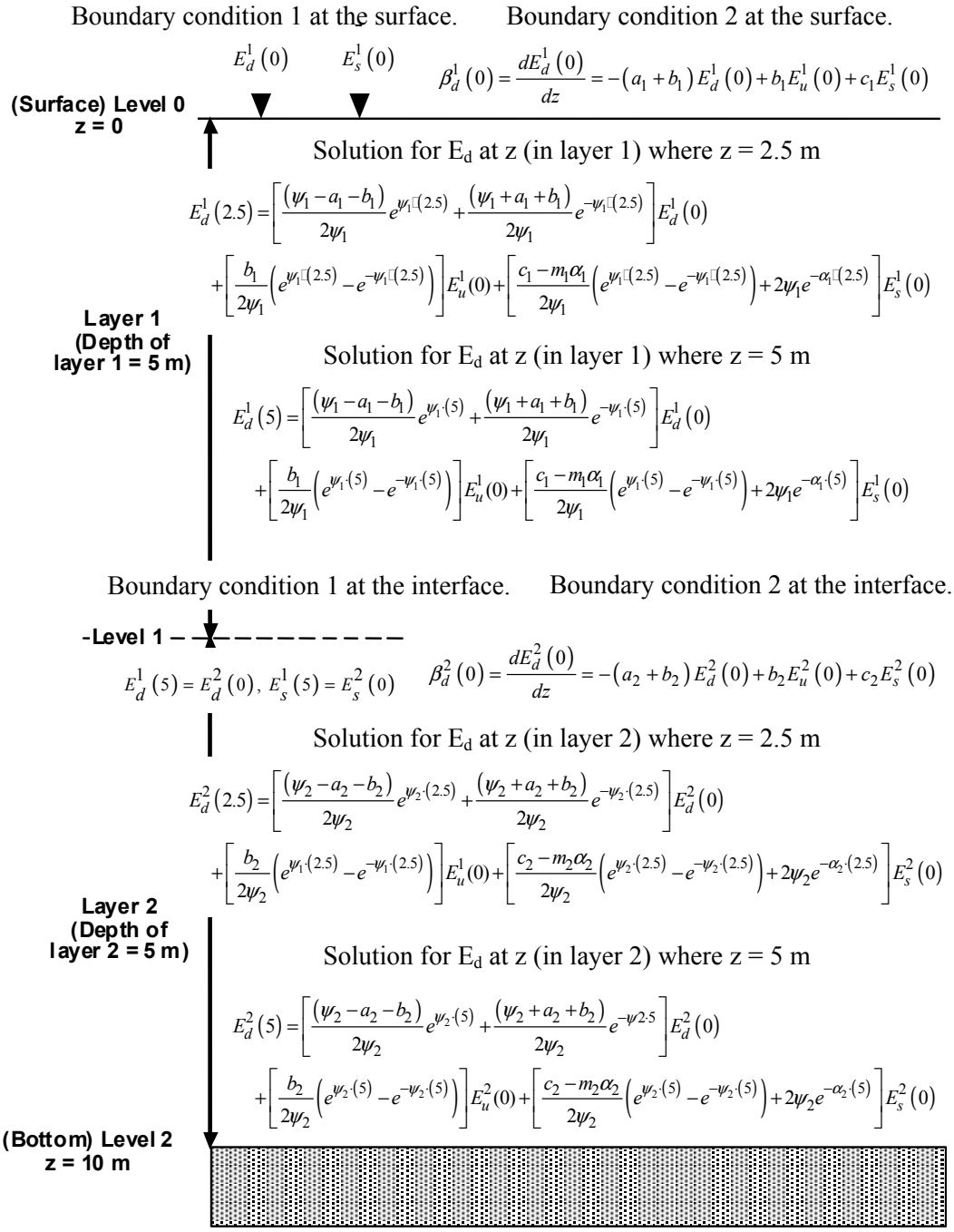


Figure 3. Sample downwelling irradiance calculations for the iterative, layered radiative transfer model.

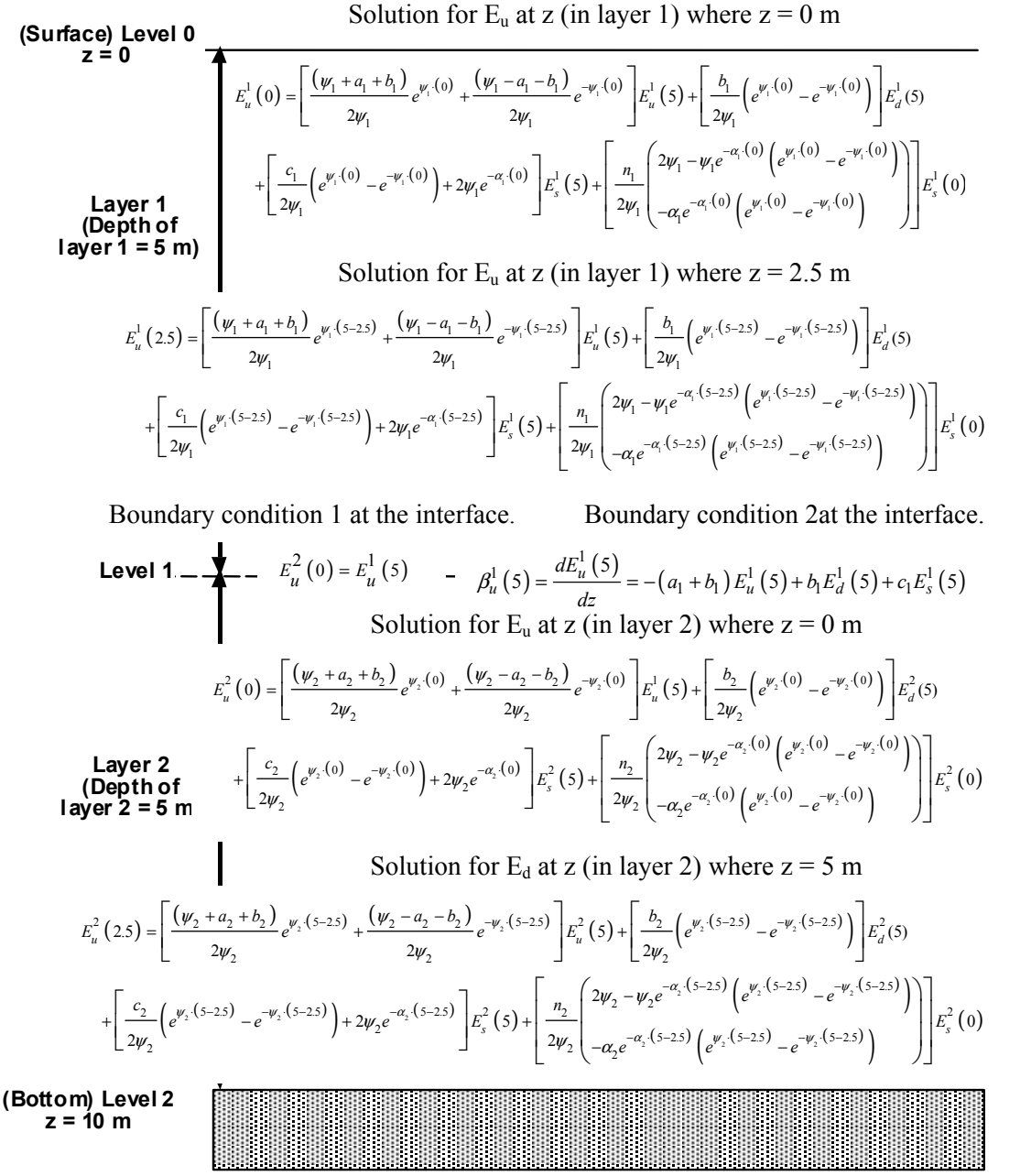


Figure 4. Sample upwelling irradiance calculations for the iterative, layered radiative transfer model.

## 3. RESULTS

Figure 5 shown below indicates the area where hyperspectral image cubes are simulated as shown in an actual aerial photo of the areas (left) and an actual airborne image (center) is within this region. The zoomed image (right) shows the presence of water surface waves in 1.3 meter pixel imagery obtained during 2003 from an altitude of approximately 3,000 feet using the AISA+ hyperspectral sensor.

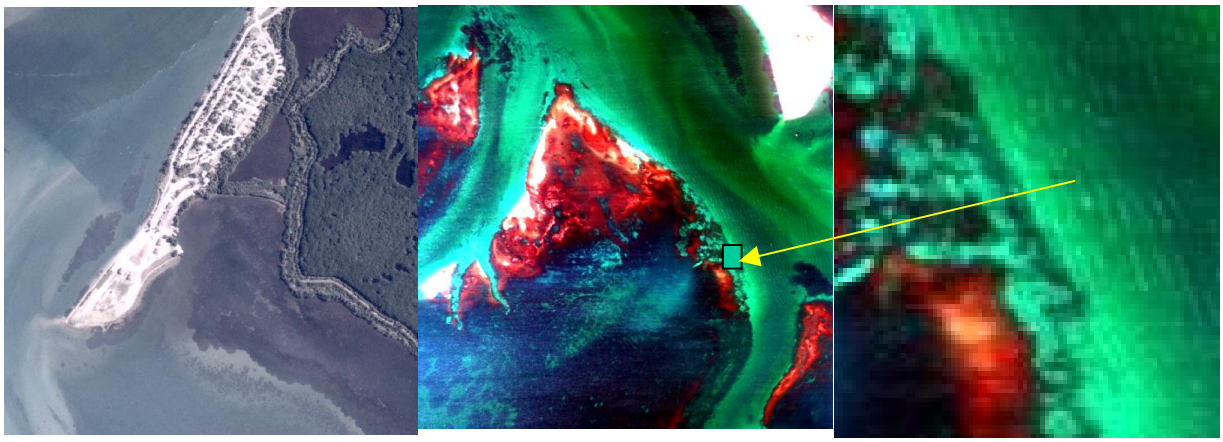

Figure 5. Actual aerial orthophoto image (left) of the Sebastian Inlet, Florida area (courtesy Robert Virnstein). Variable water depth and submerged grasses are observed. A hyperspectral image (1.3 meter resolution) image with apparent water surface waves (right) is shown from a May 29, 2003 aerial hyperspectral aerial flight.

Examples of the synthetic imagery with the MC (Monte Carlo model) and the ALIM (analytical iterative model) are shown below for cases with a smooth water surface (upper right and upper left images) and the cases of a water surface wave covered water body.

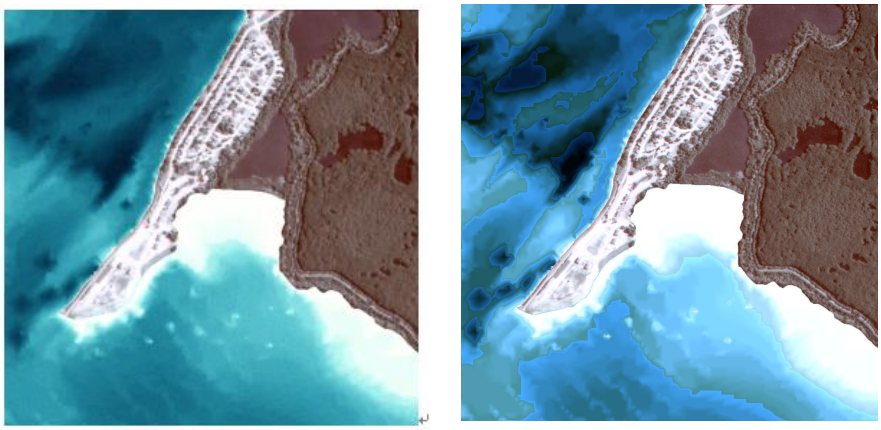

Figure 6. Synthetic image of the Sebastian Inlet area generated using the Monte Carlo model (left) and using the analytical model (right). The bottom reflectance ($R_b$) is set to 0.1. Bathymetry used was data from SJRWMD. The depth in this area is between 0-5 meters. The water column is assumed to be pure water (no chemical constituents). The model clearly shows the reflectance variations due to different water depths in the synthetic images. The white region is shallow water. Images have been contrast stretched.

Figure 7. Synthetic images of the Sebastian Inlet area generated using the Monte Carlo model (left) and using the analytical model (right) using assigned bottom reflectance ($R_b$) data as SAV bottom reflectance (Bostater, 1992). Bathymetry data used was from SJRWMD. The depth in this area is between 0-5 meters. The water column is assumed to be pure water (no chemical constituents). The dark area near the shoreline is submerged aquatic vegetation (SAV). Images have been contrast stretched and do not include water waves influences. In general, the realism of the imagery begins to be seen when realistic bathymetry is used. Next, the realism is improved by the inclusion of realistic bottom reflectance of the known features or targets. For example below is shown the effects of simulating the geographical region indicated, but where a line target has been inserted as well as showing the influence of a realistic water wave surface.

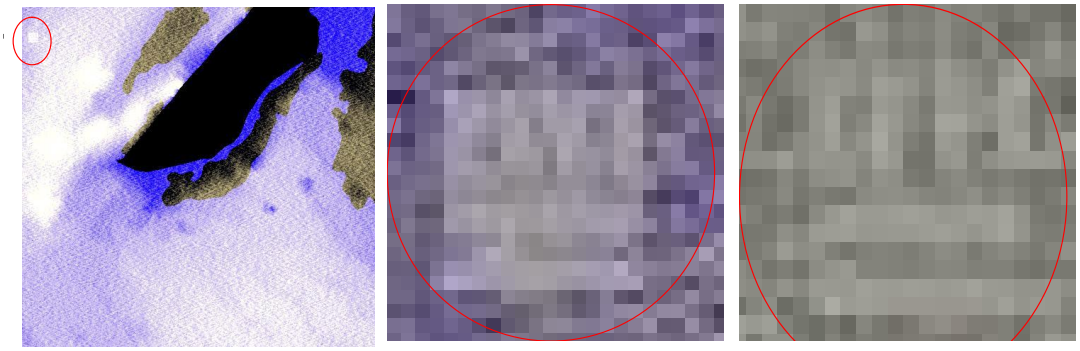

Figure 8. Synthetic image sensor simulations of a hyperspectral imaging system with continuous source illumination using a radiative transfer model (Bostater, et. al. 2000, 2004). A line target (as shown in figure 1) is simulated with 80% and 20% reflectance lines. The line target (left) is simulated as a ≈140 $cm^2$ target. The water wave surface is generated using the Philips water wave spectrum (upper middle) used in the Sebastian coastal inlet area (upper right) of the Atlantic Ocean, Florida. The wind speed is 5 $ms^{-1}$ from the NNE direction (30 $^0$). The solar zenith angle is set to 20 degrees off nadir (late morning) and the sensor viewing angle is near nadir. The bottom reflectance type in the background of the target is a seagrass or vegetative bottom type. A resulting synthetic image is presented from the clear water simulation (lower left) and the zoomed region of the panel for the target in this area (lower middle) shows the influence of the water surface and clear water column properties on the target. The lower right zoomed line target area shows the influence of wind and water quality with suspended matter of ≈ 30 $mgL^{-2}$, 20 $mgL^{-2}$ C dissolved organic matter (DOM) and chlorophyll-a pigment concentration of 20 $ugL^{-2}$.

This example shows the effects of blurring and changes in reflectance due to the water surface wave facets on the line target and the influence of water quality in the feature detection and target identification methods utilized. Other spectral wave models may be used to more accurately describe the water facet

effects, especially those developed for shallow water and those which include the effects of water wave diffraction or "wave bending". Figure 9 shown below shows the more clearly visible line target (center) located in shallow clear water in the Sebastian Inlet (right) simulation region, with the wave field generated for a 5 $ms^{-1}$ wind speed coming from $30^0$ from the North (NE wind field), with clear natural water conditions, and a sun angle of $45^0$ (mid morning) and a sensor angle of $20^{0\ off}$ nadir viewing geometry.

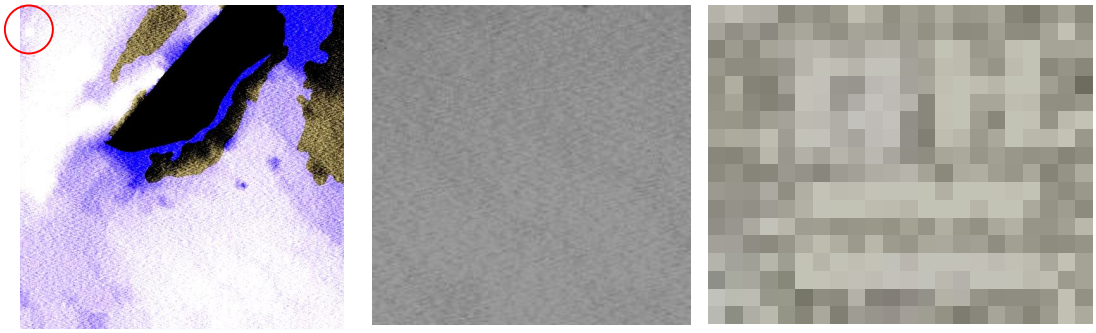

Figure 9. Hyperspectral synthetic image (left) of the Sebastian Inlet, Florida with a water surface wave field realization for a 5 $ms^{-1}$ northeast wind direction ($30^0$ NE), clear water and seagrass bottom reflectance for sun angle of $45^0$ (mid morning) and $20^0$ off nadir sensor viewing geometry. The image on the right shows the line target when image zoom and liner contrast stretching is used to see the bottom target feature under the influence of wind.

The influence of pixel size wind speed can be simulated using the Monte Carlo model. Figure 10 below shows the results of pixel size or "voxel" used on the simulation results with very little change after 12 meters and only minimal change (less than one half of a tenth of a percent in reflectance or less) and no more a tenth of 1 percent up to around 15 meters. These "adjacency affects" are thus important at small pixel sizes, however their influence appears to diminish during wind conditions as shown below, however changes are observed to vary at different wavelengths.

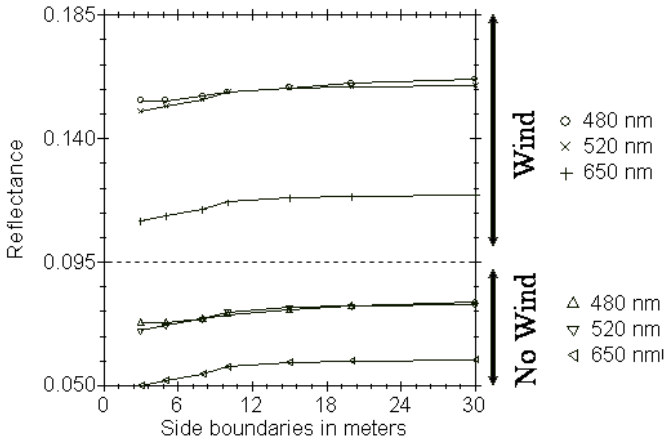


Figure 10. The influence of wind conditions and pixel sizes on simulated reflectance at 3 wavelengths as demonstrated from the Monte Carlo model results which simulate 2 flow equations shown above.

The Monte Carlo model results which are used to calculate the depth dependent nature of the light field shown in the 2 flow equations above, demonstrate the influence of wind speed (wave facets) and a nonlinear wavelength dependent effect that can be simulated with different water types (constituent concentrations) as shown in Figure 11 below.

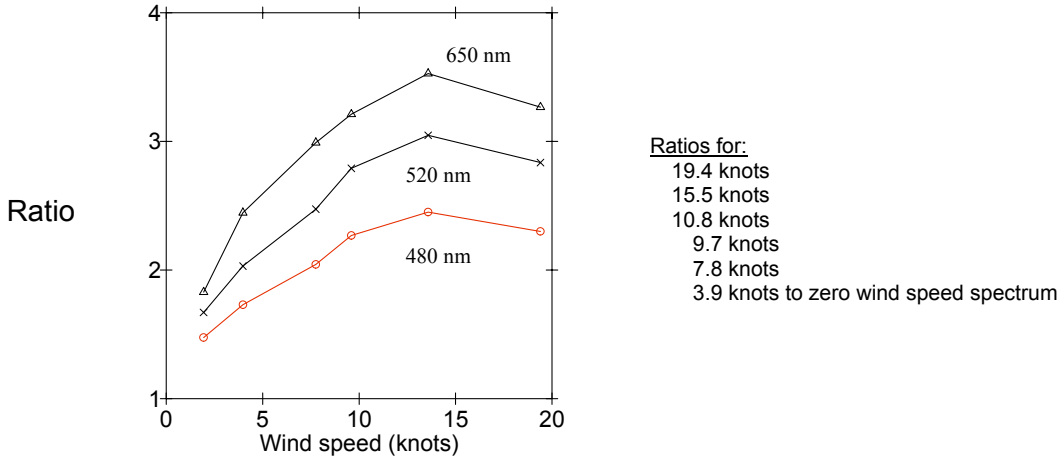


Figure 11. Ratio of reflectance from MC model at 480nm, 520 nm, 650nm driven with wind at various wind speeds normalized to no wind speed reflectance. Bottom reflectance type is seagrass, water depths were ≈ 4 m, chlorophyll-a concentration assumed was 1.0 $\mu gL^{-1}$ DOM (dissolved organic matter) of 5.0 mg C $L^{-1}$ and suspended sediments (seston) concentration of 0.05 $mgL^{-1}$.

## 4. CONCLUSION

Methods for simulating synthetic realistic water wave surfaces to a water volume, layered, radiative transfer model to create synthetic images has been demonstrated and also applied to a Monte Carlo radiative transfer developed in our lab. Applying this methodology has some advantages, which are: (1) synthetic images are very useful for remote sensing algorithm testing, e.g., by creating a synthetic image one can test whether mathematical reflectance models of a water body accurately captures the dominant factors that cause a particular reflectance pattern or signature due to a subsurface feature or target; (2) the total water surface reflectance includes reflectance due to surface waves, reflectance due to pure water, reflectance due to water constituents, and reflectance due to bottom type. Future research will include determining the effects of the fetch due to wind, to the use of the Jonswap model and other models which will allow for shallow water surface wave refraction effects on submerged feature extraction from hyperspectral imagery. These techniques we believe will enhance our capabilities for design of future sensors as well as for use in environmental monitoring (e.g. submerged vegetative cover), and other features or targets in water.**ACKNOWLEDGMENTS**

Funding for various aspects of this research was associated with the following organizations:
The Link Foundation, NASA Stennis Space Center, St. Johns River Water Management District, Northrop Grumman Corporation, KB Sciences and S & C Services.

## REFERENCES


1. Mastin, Gary A., Peter A. Watterger, and John F. Mareda, “Fourier Synthesis of Ocean Scenes”, IEEE CG&A, March 1987, pp. 16-23.
2. Tessendorf, Jerry, “Simulating Ocean Water,” SIGGRAPH 2001 Course notes, http://home1.gte.net/tssndrf/index.html, 19 pp.
3. Premoze, S., Ashikhmin, A., “Rendering Natural Waters,” In: *Eighth Pacific Conference on Computer Graphics and Applications*, Hong Kong, 3-5 October, 2000, pp.23-30.
4. Jensen, L. S., Goliáš, Robert, “Deep Water Animation and Rendering,” http://www.swrendering.com/papers/deep_water_animation_and_rendering.pdf, 13 pp.
5. Chen, Gottfried, “CHENGINE,” http://gchen.sdf-eu.org/Chengine/Pages/Diary.htm , 2002.
6. Hilgart, Mark, “Real-time Statistical Wave Implementation using IFFTs,” http://www.markhilgart.com/tex/waves/ , 2002.
7. Gregg, W., Carder, K., “A simple spectral solar irradiance model for cloudless marine atmospheres,” *Limnology & Oceanography*, Vol. 35(8), pp. 657-675, 1990.
8. Koepke, P. (1984), “Effective Reflectance of Oceanic Whitecaps,” *Applied Optics*, 23, 1816-1824.
9. Ma, W. (1997), "An Analytical Two-Flow Model to Simulate the Distribution of Irradiance in Coastal Waters with a Wind-Roughened Surface and Bottom Reflectance," PhD Dissertation, Florida Institute of Technology, Department of Marine and Environmental Systems.
10. Preisendorfer, R. W. (1957), "Exact Reflectance under a Cardiodal Luminance Distribution," *Quarterly Journal of the Royal Meteorological Society*, 83, 540.
11. Jerlov, N. G. (1976), *Marine Optics*, Amsterdam: Elsevier Scientific Publishing Company.
12. Preisendorfer, R. W. (1976), *Hydrologic Optics*, Honolulu, Hawaii: U. S. Department of Commerce, National Oceanic and Atmospheric Administration, Environmental Research Laboratories, Pacific Marine Environmental Laboratory.
13. Burt, W. V. (1954), “Albedo over Wind-Roughened Water,” *Journal of Meteorology*, 11, 283-290.
14. Bostater, C. and A. Lamb, “Innovative use of in-situ and airborne measurements of electromagnetic radiation in near shore environments,” In: *Proc. 2nd Intl. Conference on Spectral Remote Sensing Research*, San Diego, CA, USACOE, July 1994, pp. 673-682.
15. Bostater, C., W. Ma, T. McNally, M. Gimond, and A. P. Lamb, “Application of an optical remote sensing model,” In: *Proceedings of the European Optical Society and SPIE – The International Society for Optical Engineering (EUROPTO), The European Symposium on Satellite Remote Sensing*, Paris, France, 25-28 September, 1995, Volume 2586, pp. 32-43.
16. Bostater, C., and L. Huddleston, “Layered analytical radiative transfer model for simulating water color of coastal waters and algorithm development,” In: *Proceedings of the European Optical Society and SPIE – The International Society for Optical Engineering (EUROPTO), Remote Sensing of the Ocean and Sea Ice 2000*, Barcelona, Spain, 28-29 September, 2000, Volume 4172, pp. 153-161.
17. Bostater, C., L. Huddleston, and M. Tepel, “Improvements to a layered analytical irradiance model for application to coastal waters with depth dependent water constituents, various bottom types, and variable water depths,” In: *Proceedings of the European Optical Society and SPIE – The International Society for Optical Engineering (EUROPTO), Remote Sensing of the Ocean and Sea Ice 2001*, Toulouse, France, 18 and 20-21 September, 2001, Volume 4544, pp. 236-245.
18. Bostater, C., L. Huddleston, C. Semmler, and J. Mieles, “An iterative algorithm for layered optical remote sensing reflectance modeling of natural waters with depth dependent aquatic constituent concentrations,” In: *Proceedings of the European Optical Society and SPIE – The International Society for Optical Engineering (EUROPTO), Remote Sensing of the Ocean and Sea Ice 2002*, Agia Pelagia, Crete, Greece, 24 September, 2002, Volume 4880, pp. 88-101.